Geotechnical and Structures Laboratory

**US Army Corps
of Engineers**®
Engineer Research and
Development Center

Mesoscale Modeling of Cementitious Materials: Phase I

Mei Qiang Chandler, William B. Lawrimore,
Micael C. Edwards, Robert D. Moser, Jameson D. Shannon,
and James L. O'Daniel

May 2019

The U.S. Army Engineer Research and Development Center (ERDC) solves the nation's toughest engineering and environmental challenges. ERDC develops innovative solutions in civil and military engineering, geospatial sciences, water resources, and environmental sciences for the Army, the Department of Defense, civilian agencies, and our nation's public good. Find out more at www.erdc.usace.army.mil.

To search for other technical reports published by ERDC, visit the ERDC online library at http://acwc.sdp.sirsi.net/client/default.

Mesoscale Modeling of Cementitious Materials: Phase I

Mei Qiang Chandler, William D. Lawrimore, Micael C. Edwards, Robert D. Moser, Jameson D. Shannon, and James L. O'Daniel

Geotechnical and Structures Laboratory
U.S. Army Engineer Research and Development Center
3909 Halls Ferry Road
Vicksburg, MS 39180-6199

Abstract

Cementitious materials such as concrete are intrinsically heterogeneous and include internal structures and constituents across length scales ranging from nanometers to millimeters. These materials are widely used as protective materials for military applications. They need not only to withstand conventional quasi-static loadings but also to defeat extreme loadings such as high-rate blast, impact, and penetration. To fully explore the design and application of these materials in war-fighting efforts, it is essential to understand the deformation and failure mechanisms of multiscale internal structures and constituents under different loading conditions. Mesoscale structures and constituents of cementitious materials include mesoscale particles such as aggregates, sand, fibers, mesoscale porosities, and cracks. Several numerical methods have been developed to investigate the deformation and failure mechanisms of mesoscale structures and constituents under different loading conditions. In this report, we explored the Lattice Discrete Particle Method (LDPM) and the Finite Element Method (FEM). The work provides some basic knowledge on these methods and aids in formulating a path forward in the next phase of the research.

Contents

Figures and Tables

Figures

Tables

Preface

This study was conducted for Headquarters, U. S. Army Corps of Engineers under Project Number 465387, the "Military Engineering Research Program." The Technical Monitor was Ms. Pamela G. Kinnebrew, Technical Director for Military Engineering, U.S. Army Engineer Research Development Center (ERDC). Dr. Robert D. Moser of the ERDC Geotechnical and Structures Laboratory (ERDC-GSL) was the Technical Manager.

The work was performed by the Structural Mechanics Branch (GSM), Geosciences and Structures Division (GS), and the Concrete and Materials Branch (GMC), Engineering Systems and Materials Division (GM), ERDC-GSL. At the time of publication, Mr. Bradford A. Steed was Chief, CEERD-GSM; Mr. Christopher M. Moore was Chief, CEERD-GMC; Mr. James L. Davis was Chief, CEERD-GS; Mr. Justin Strickler was Acting Chief, CEERD-GM; and Mr. R. Nicholas Boone, CEERD-GZT, was Technical Director for Force Projection and Maneuver Support. The Deputy Director of ERDC-GSL was Mr. Charles Ertle II, and the Director was Mr. Bartley P. Durst.

COL Ivan P. Beckman was the Commander of ERDC, and Dr. David W. Pittman was the Director.

Unit Conversion Factors

Multiply	By	To Obtain
degrees (angle)	0.01745329	radians
degrees Fahrenheit	(F-32)/1.8	degrees Celsius
megahertz (MHz)	1.0 E+06	hertz
kilohertz (kHz)	1.0 E+03	hertz
feet	0.3048	meters
inches	0.0254	meters
knots	0.5144444	meters per second
microns	1.0 E-06	meters
nanometers (nm)	1.0 E-09	meters
miles (nautical)	1,852	meters
miles (U.S. statute)	1,609.347	meters
miles per hour	0.44704	meters per second
ounces (mass)	0.02834952	kilograms
pounds (mass)	0.45359237	kilograms
square feet	0.09290304	square meters
square inches	6.4516 E-04	square meters
square miles	2.589998 E+06	square meters
square yards	0.8361274	square meters
yards	0.9144	meters

1 Introduction

1.1 Background

Concrete is a composite material with complex internal structures across multiple length scales. For normal-strength concrete, coarse aggregates with dimensions ranging from 5 to 40 mm are embedded in a mixture of finer aggregates, sand, and cement paste. The finer aggregates and sand with dimensions ranging from 0.05 to 5 mm are embedded in a mixture of unhydrated cement particles and hydrated products. Hydrated products include gel phases such as calcium silicate hydrate (Allen et al. 2007) and crystalline phases such as ettringite and calcium hydroxide. Pores and cracks with sizes ranging from nanometers to millimeters are present in normal-strength concrete (Mehta and Monteiro 2014). For ultra-high performance concrete (UHPC), coarse aggregates, millimeter-sized cracks, and large pores are generally absent. Fibers with lengths ranging from a few to tens of millimeters are sometimes included in UHPC to improve its ductility (Williams et al. 2009). Under loading, concrete exhibits complex deformation, damage, and failure mechanisms such as microcracking, interface debonding, pore collapse, particle fracturing, and material compaction and crushing (Nemati 1997; Calixto 2001). When fibers are present, the damage and deformation mechanisms also include fiber pull-out, fiber breakage, and crack-bridging (Oesch 2016; Landis et al. 2019). Different loading conditions will induce different deformation and failure mechanisms at different length scales (Vegt et al. 2007; Moser et al. 2013). It is essential to investigate multiscale deformation and failure mechanisms under different loading conditions in order to effectively design protective materials and systems for differing threats.

Macroscale continuum models treating concrete as a homogenous material have been widely used to analyze the responses of concrete and to aid in the design of concrete structures under different loading conditions (Adley et al. 2010; Fossum and Brannon 2016; Bazant et al. 2000; Canner and Bazant 2000). These models aim to capture the basic material behaviors of concrete by formulating deformation, damage, and failure phenomenologically. Because macroscale constitutive equations are not linked with structures and mechanisms from lower length scales, their capability to optimize the materials at different length scales for better performance is limited. To optimize the design of cementitious materials

for the performance of the concrete structure under different loading conditions, the particular challenges are how to associate the materials process parameters -- such as selections of cement, water/cement ratio, fly ash, silica flour, sand, and aggregate information -- to the material properties and behavior of concrete. Numerical models such as CEMHYD3D (three-dimensional cement hydration and microstructure development modeling package; Bentz 2005) have been developed to predict the microstructure of the cement paste. Experimental characterization tools such as X-ray tomography (Micro-CT), optical microscopy (OM), and scanning electron microscopy (SEM) have been applied to probe the meso/microscale structures of concrete (Scott et al. 2015; Oesch 2016).

Several modeling methods have been developed to investigate the material responses of the concrete at micro/mesoscale. Schlangen and Garboczi (1997) applied lattice models to study the fracture process of concrete at microscale (cement paste) and mesoscale (mortar/aggregates). Lattice models discretize materials as a network of springs or beams. Fracture is simulated by removing lattice elements in which load or energy exceeds certain criteria. These types of models have difficulties in capturing the compressive behavior of cementitious materials, particularly under high confinement (Cusatis et al. 2003).

Finite element models (Zhou et al. 2017; Jin et al. 2017; Qsymah et al. 2017) have been applied in mesoscale simulations by treating concrete as a three-phase material (i.e., aggregates, interfacial transition zone, and mortar). Different constitutive equations are applied to different phases. Failure is based on the continuum damage mechanics concept. Besides the difficulties in modeling softening behavior, another difficulty of these types of methods is formulating suitable constitutive equations and calibrating material constants.

Discrete element methods have also been applied in modeling cementitious materials at the mesoscale (Sinaie 2017; Jin et al. 2017; Suchorzewski et al. 2017). In these types of models, aggregates and mortar phases are represented by bonded particles. The failure process is modeled by breaking the bonds between particles. The difficulties in these types of models involve defining the particle sizes, particle packing, formulating interparticle forces, and calibrating material constants.

The Lattice Discrete Particle Method (LDPM) (Cusatis et al. 2003 and 2011; Ashari et al. 2017) was developed by researchers at Northwestern University and Engineering System Solutions in collaboration with the Geotechnical and Structures Laboratory at the U.S. Army Engineer Research and Development Center (ERDC). In these models, aggregates and particles were explicitly modeled as rigid particles. The mortar or paste between aggregates is represented by a number of facets, which connect the particles. Constitutive laws are applied on the facets to simulate the interactions between aggregates through the mortar and the cement paste. The parameters of the constitutive laws are calibrated from laboratory tests of concrete specimens. In the current LDPM implementation, the interfacial transition zone (ITZ) is not modeled explicitly, and aggregates cannot fracture.

There are many pre-existing multiscale cracks in cementitious materials. The failure process involves multiscale crack growth and coalescence (Calixto 2001; Mayercsik 2015). Mayercsik (2015) applied the micro-mechanical damage model developed by Paliwal and Ramesh (2008) on ceramic materials. The micro-mechanical damage model is based on frictional sliding and growth of pre-existing cracks and is a function of size and distribution of pre-existing cracks and flaws. Lin et al. (2016) constructed a unit cell model explicitly modeling pores from X-ray tomography and evaluated macroscale damage evolution by calculating the reduction of Helmholtz free energy of a unit cell induced by crack growth from pre-existing microcracks. Lin et al.'s work is an extension of the work by Ren et al. (2010).

1.2 Objective

The objective of this work is to examine in detail the basic features and the state of the art of two mesoscale modeling methods. One is the particle-based LDPM, and the other is the continuum-based finite element method (FEM). By investigating the basic features of these two methods, a path forward in the next phase of the research is formulated.

2   Mesoscale Modeling with LDPM

2.1   Basic LDPM theory

The basic equations of LDPM are included in this section. Cusatis et al. (2003; 2011) give an in-depth description of the method development and equations. LDPM was initially developed to model cementitious materials, including the size distributions of aggregates. Each aggregate is approximated as a sphere, and these spheres are randomly placed within the prescribed volume of the sample but in accordance with aggregate size distribution of the concrete material being simulated. The particle size distribution d is related to the minimum diameter d_o and maximum diameters d_a of aggregates, as well as sieve curve parameters of the mix design, by using equation 2.1.

$$f(d) = \frac{q d_0^q}{\left[1 - (\frac{d_0}{d_a})^q\right] d^{q+1}}$$
2.1

The cumulative distribution function is expressed as

$$P(d) = \int_{d_0}^{d} f(d) \Delta d = \frac{1 - (\frac{d_0}{d})^q}{1 - (\frac{d_0}{d_a})^q}$$
2.2

The sieve curve is expressed as

$$F(d) = (\frac{d}{d_a})^{n_F}$$
2.3

and nF is a function of q

$$n_F = 3 - q$$
2.4

where q is a material parameter. When q is equal to 2.5, and n_F is equal to 0.5, $F(d)$ is the Fuller curve.

Delaunay tetrahedralization is applied to particle centers to define a three-dimensional mesh of tetrahedrals. Delaunay tessellation is applied to create a system of polyhedral cells. Facets are created to represent potential crack surfaces of the mortar or paste. Polyhedral cells interact with each other through facets at the contact area, and rigid-body kinematics is adopted to describe the displacement of each cell. The displacement of the contact point of facets **u(x)** is defined as

$$u(X) = u_i + \theta_i \times (X - X_i) = A_i(X)Q_i$$
2.5

$$A_i(x) = \begin{bmatrix} 1 & 0 & 0 & 0 & x_3 - x_{3i} & x_{2i} - x_2 \\ 0 & 1 & 0 & x_{3i} - x_3 & 0 & x_1 - x_{1i} \\ 0 & 0 & 1 & x_2 - x_{2i} & x_{1i} - x_1 & 0 \end{bmatrix}$$ 2.6

$$Q_i^T = [u_i^T \quad \theta_i^T], u_i^T = [u_{1i} \quad u_{2i} \quad u_{3i}] \; \theta_i^T = [\theta_{1i} \quad \theta_{2i} \quad \theta_{3i}]$$ 2.7

Figure 1. Single LDPM particle and associated facets.
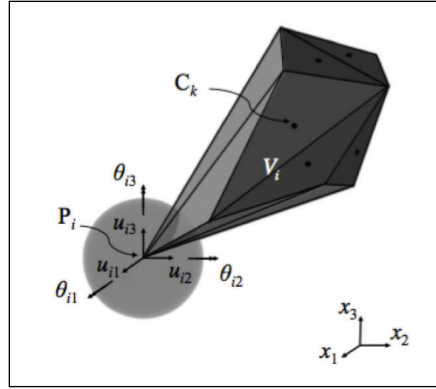
where $\mathbf{u_i}$ is the displacement vector of the particle centroid, $\mathbf{\theta_i}$ is the rotational vector of the cell, $\mathbf{x}$ is the coordinate vector of the contact points, and $\mathbf{x_i}$ is the coordinate vector of the particle centroid. Figure 1 shows a particle and its associated facets.

Stresses and strains are defined at the centroid of each facet. The strains $\mathbf{\varepsilon}$ at the facet in the normal direction $\mathbf{n}$, shear directions $\mathbf{m}$ and $\mathbf{l}$ are calculated as

$$\varepsilon_N = \frac{n^T[u_c]}{L_e}, \quad \varepsilon_M = \frac{m^T[u_c]}{L_e}, \quad \varepsilon_L = \frac{l^T[u_c]}{L_e}$$ 2.8

where $\mathbf{u_c}$ is the displacement jump at each facet centroid between two adjacent cells, and L_e is edge length of the facet.

Elastic stresses $\mathbf{\sigma}$ in the normal and shear directions are calculated as

$$\sigma_N = E_N \varepsilon_N \;, \quad \sigma_M = E_T \varepsilon_M, \quad \sigma_L = E_T \varepsilon_L$$ 2.9

When tensile normal strain is greater than zero, the following damage-like relationships are used

$$\sigma_N = \sigma \frac{\varepsilon_N}{\varepsilon}, \quad \sigma_M = \sigma \frac{\alpha \varepsilon_M}{\varepsilon}, \quad \sigma_L = \sigma \frac{\alpha \varepsilon_L}{\varepsilon}$$ 2.10

$$\varepsilon = \sqrt{\varepsilon_N^2 + \alpha(\varepsilon_M^2 + \varepsilon_L^2)}\sigma = \sqrt{\sigma_N^2 + (\sigma_M^2 + \sigma_L^2)/\alpha} \qquad 2.11$$

where α is the shear-normal coupling parameter. When strains exceed the elastic limit, a crack opening is created along the facet.

The stress-strain boundary equation is used to describe the constitutive relations

$$\sigma_{bt}(\varepsilon, \omega) = \sigma_0(\omega)\exp\left[-H_0(\omega)\frac{\langle \varepsilon_{max}-\varepsilon_0(\omega)\rangle}{\sigma_0(\omega)}\right] \qquad 2.12$$

where ω is a variable defining the coupling between shear and normal loading, ε_{max} is the maximum effective strain, σ_o is the effective strength, and $H_o(\omega)$ is the softening modulus.

A strain-dependent normal boundary equation is used to describe pore collapse and compaction.

$$\sigma_{bc}(\varepsilon_D, \varepsilon_V) = \begin{cases} \sigma_{c0} & for \ -\varepsilon_V \le 0 \\ \sigma_{c0} + \langle -\varepsilon_V - \varepsilon_{c0}\rangle H_c(r_{Dv}) & for \ 0 \le \varepsilon_{DV} \le \varepsilon_{C1} \\ \sigma_{c1}(r_{DV})exp[(-\varepsilon_V - \varepsilon_{c1})H_c(r_{DV})/\sigma_{c1}(r_{DV})] & otherwise \end{cases} \qquad 2.13$$

where $r_{DV} = \frac{\varepsilon_D}{\varepsilon_V}$, $\varepsilon_D = \varepsilon_N - \varepsilon_V$, and ε_V is volumetric strain, $\varepsilon_{DV} = \varepsilon_V + \beta\varepsilon_D$; β is a material parameter, σ_{c0} is the mesoscale yielding compressive stress, $\varepsilon_{c0} = \sigma_{c0}/E_0$ is the compaction strain at the onset of pore collapse, $H_c(r_{DV})$ is the initial hardening modulus, $\varepsilon_{c1} = K_{c0}\varepsilon_{c0}$ is the compaction strain at which rehardening begins, and $\sigma_{c1}(r_{DV}) = \sigma_{c0} + (\varepsilon_{c1} - \varepsilon_{c0})H_c(r_{DV})$.

Shear strength is defined as a function of negative normal stress, cohesion, and friction coefficient.

$$\sigma_{bs}(\sigma_N) = \sigma_s + (\mu_0 - \mu_\infty)\sigma_{N0} - \mu_\infty\sigma_N - (\mu_0 - \mu_\infty)\sigma_{N0} \times \exp(\frac{\sigma_N}{\sigma_{N0}}) \qquad 2.14$$

where σ_s is the cohesion and σ_{No} is the normal stress at which the internal friction coefficient transitions from μ_o and μ_∞.

Translational displacement $\boldsymbol{u}$ and rotational displacement $\boldsymbol{\theta}$ of each particle are defined as

$$M_u^I \ddot{u}^I - V^I b^0 = \sum_{F_I} A t^{IJ} \quad , \quad M_\theta^I \ddot{\theta}^I = \sum_{F_t} A c^I \times t^{IJ} \qquad 2.15$$

where M_u^I is the mass of particle I, $\boldsymbol{V^I}$ is the velocity vector of particle I, b^0 is the damping coefficient, M_θ^I is the mass moment inertia of particle I, t^{IJ} is the unit contact force vector imposed from J particle to I particle, C^I is the vector from the center of the particle I to the contact point, and A is the contact area at the facet.

A recent development is the ability to explicitly model pores as voids in the model.[*] The pores are distributed in a manner similar to the aggregate particles, based on minimum and maximum pore size, total porosity, and Fuller curve coefficient. With explicit porosity, some tetrahedrals will have a pore at a corner. The tetrahedralization process (Figure 2) will then move the affected facets to the surface of the pore. This process increases the number of nodes.

Figure 2. Tetrahedralization process for pores.
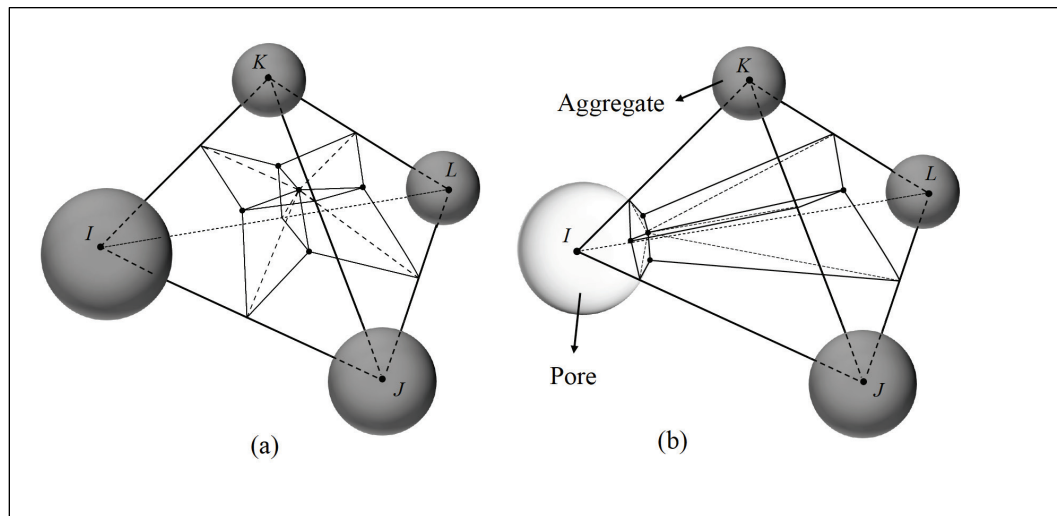
2.2   Model setup

This section details LDPM applied to simulate the response of ultra-high-performance concrete (UHPC) without fibers under compression and tension loading. Mesoscale porosities were also inserted in the model to study the effects of mesoscale porosities on the tensile and compressive responses of UHPC. Figure 3 shows SEM images of the mesoscale structure of a UHPC developed by ERDC (Williams et al. 2009). In this model, rigid spheres were used to represent sand particles. The size distributions of the sand particles, based on Burcham (2016), were used to

---

[*] Cusatis, G. 2017. *Task 3 further development and validation of the Lattice Discrete Particle Model (LDPM).* Project ID 60043148: Contract Report.

generate the rigid particles. In one case, mesopores were not inserted into the model. In another case, mesopores were inserted into the model. The size distributions of mesopores, based on Burcham (2016), were applied to generate the mesopores explicitly in the model. Figure 3 also shows the polyhedral cell representation of the model without and with mesopores.

Figure 3. The SEM image shows the distributions of sand particles and mesopores in a UHPC specimen. In the LDPM model setup, sand particles were represented as rigid particles, and mesopores were inserted into the model explicitly.
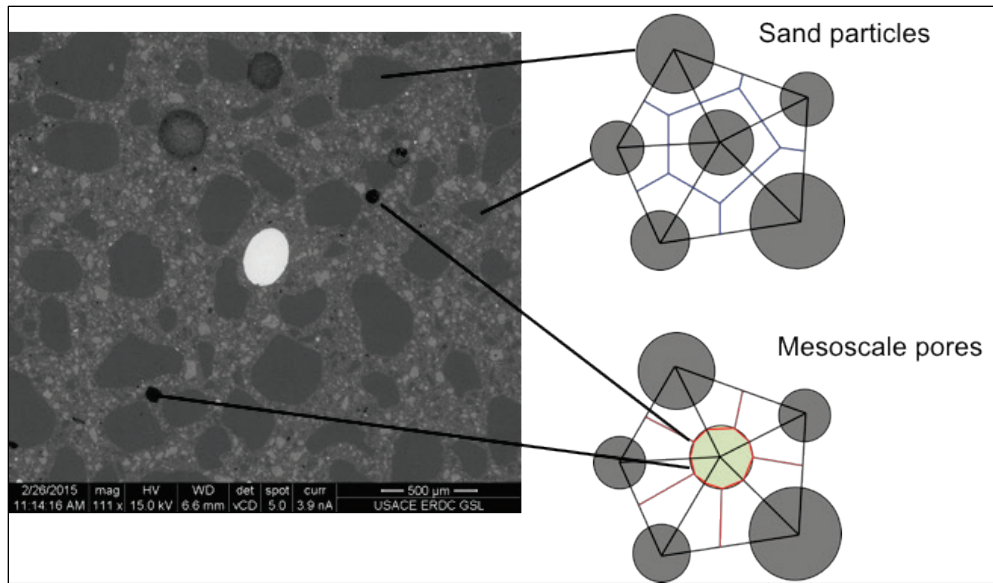
Table 1 lists the parameters applied in the models. The mix design properties were used to generate particles and porosities in the models. Note that the average size of the sand and mesopores is on the order of 0.5 mm, and the sizes of the sand and mesopores assigned in the table were from 2 mm to 4 mm. The larger particle and pore sizes were used to reduce the computation time. However, the material properties' parameters were adjusted based on the particle and pore sizes. The material property parameters were fitted based on experimental test data such as hydrostatic compression, unconfined compression, compression under low confinement, and compression under high confinement described in Williams et al. (2009) for Cor-Tuf without fibers. The fitting procedure refers to Mencarelli (2007). The specimen size in all simulations was 25-mm in radius and 50-mm in height. Figure 4 shows the cylinder geometry with facets (left) and particles (right) for the specimen without pores. Figure 5 shows the cylinder with 5% porosity. In the specimen without pores, a total 2,841 particles and 13,928 facets were created. In the specimen with pores, 3,957 particles; 446 pores; and 20,185 facets were created.

The displacement in the uniaxial compressive simulations was applied at a rate of 10 mm/s, while the displacement in the uniaxial tension simulations was applied at a rate of 1 mm/s. The displacement was applied to the nodes of the top of the sample while the base was fixed in the axial direction.

Table 1. LDPM material parameters.

Material CorTuf LDPM	
Mix Design Parameters	
1 Cement Content	789.1 kg/m3
2 Water To Cement Ratio	0.2082
3 Aggregate To Cement Ratio	1.9432
4 Min Aggregate	2 mm
5 Max Aggregate	4 mm
6 Fuller Coefficient	0.5
7 Pore Min	2 mm
8 Pore Max	4 mm
9 Pore Fuller Coefficient	0.5
10 Porosity	0.05
Static Parameters	
11 Normal Modulus	31250 MPa
12 Densification Ratio	2.5
13 Alpha	0.25
14 Tensile Strength	3 MPa
15 Compressive Strength	500 MPa
16 Shear Strength Ratio	17
17 Tensile Characteristic Length	150 mm
18 Softening Exponent	0.2
19 Initial Hardening Modulus Ratio	0.36
20 Transitional Strain Ratio	2
21 Initial Friction	0.5
22 Asymptotic Friction	0
23 Transitional Stress	300 MPa
24 Volumetric Deviatoric Coupling	0
25 Deviatoric Strain Threshold Ratio	2
26 Deviatoric Damage Parameter	1

Figure 4. The image on the right represents the sand particles of different sizes. The image on the left represents the facets between particles.
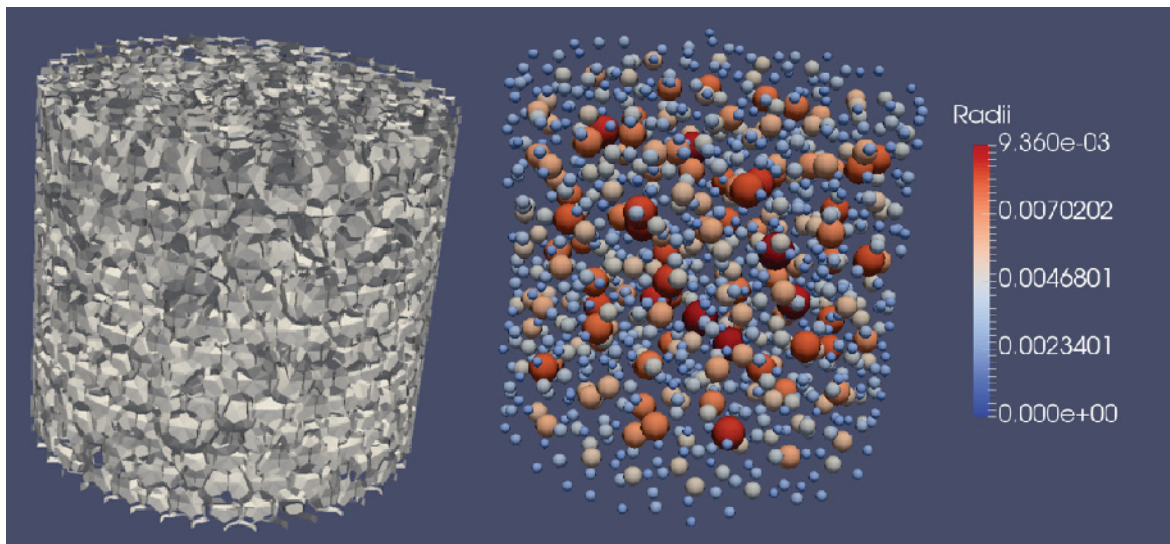
Figure 5. The spheres in darker color represent the sand particles while spheres in light color represent the mesopores.
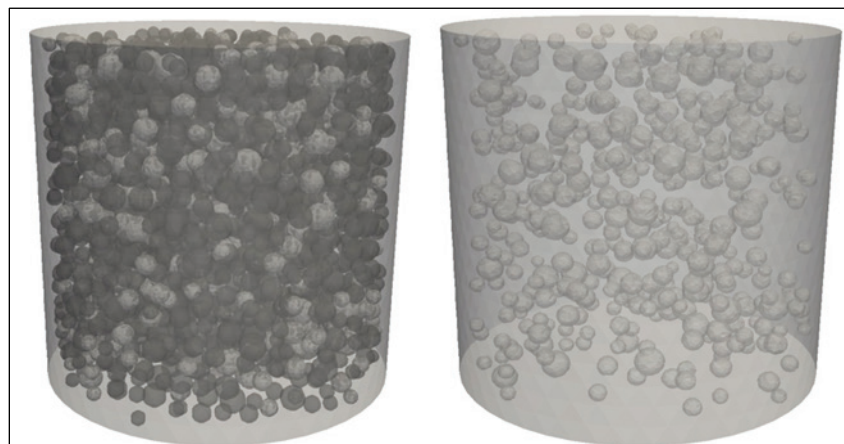
2.3   Results and discussion

Figure 6 shows the stress/strain curve and corresponding snapshots of crack opening from uniaxial compression simulations without mesopores. Note the unit of crack opening is in millimeters. Figure 6 shows that the specimen exhibited a brittle failure mode, and the cracks initiated from the top surface and propagated vertically until the failure. This failure process agrees with the experimental observation of cylindrical specimens under uniaxial compression performed by Scott et al. (2015), which is also shown in Figure 6. Figure 7 shows the stress/strain curve and corresponding snapshots of crack opening for the specimen with mesopores under uniaxial compression simulations. Figure 7 shows that the specimen with

mesopores exhibited similar brittle failure mode and that the cracks initiated from the top of the surface and propagated vertically until failure. However, close examination of the crack opening results shows that cracks initiated from the mesopores near the surfaces and grew along the mesopores until the final failure. This failure mechanism agrees well with experimental observations for quasi-brittle materials (Liu et al. 2017).

Figure 8 shows the stress/strain curve and corresponding snapshots of crack opening for the specimen without mesopores under uniaxial tension. Figure 8 shows that cracks initiated at the circumferential surface of the specimen and grew perpendicular to the loading directions until failure at two locations. Figure 9 shows the stress/strain curve and corresponding snapshots of crack opening for the specimen with mesopores under uniaxial tension. Figure 9 shows that cracks initiated at the mesopores near the boundary and grew from pore to pore in the direction that was perpendicular to the loading direction until final failure.

Figures 10 and 11 show a comparison of stress/strain curves of the specimen with and without mesopores under uniaxial compression and tension, respectively. Figure 10 shows that including 5% porosity in volume with sizes comparable to those of particles explicitly in the model reduced the elastic modulus by 12% and the peak stress by 30% under uniaxial compression. Figure 11 shows that including 5% porosity with sizes comparable to those of particles explicitly in the model reduced the elastic modulus by 14%, and the peak stress by 21% under uniaxial tension. These results suggest that mesoscale porosities are detrimental to both compressive and tensile properties of UHPC. Based on Liu et al. (2017), the elastic modulus for porous quasi-brittle materials is a function of volumetric percentage of porosity.

$$E = E_0 e^{-b_E P_V} \qquad\qquad 2.16$$

where E is the elastic modulus with pores, E_0 is the elastic modulus without pores, P_V is volume fraction of porosity, and b_E is a material parameter. Based on the data from the LDPM simulations, b_E is calculated to be 2.55 for the compressive test and 3.0 for the tensile test. These numbers are comparable with those of ceramic (Liu et al. 2017) for similar porosity levels. Based on Liu et al. (2017), the strength with a certain porosity level is also related to pore-free strength, as

$$\sigma = \sigma_0 e^{-b_\sigma P_V} \qquad\qquad 2.17$$

where σ is the strength with pores, σ_0 is the strength without pores, P_V is volumetric percentage of porosity, and b_σ is a material parameter. Based on the data from the LDPM simulations, b_σ is calculated to be 7.13 for the compressive test and 4.7 for the tensile test. These numbers are much higher than those of ceramic with a similar porosity level. More simulations need to be performed for different porosity levels to test whether equations 2.16 and 2.17 can be applied to UHPC with different porosity levels.

Figure 6. The stress/strain curve and corresponding snapshots of crack opening for the specimen without mesopores under uniaxial compression.
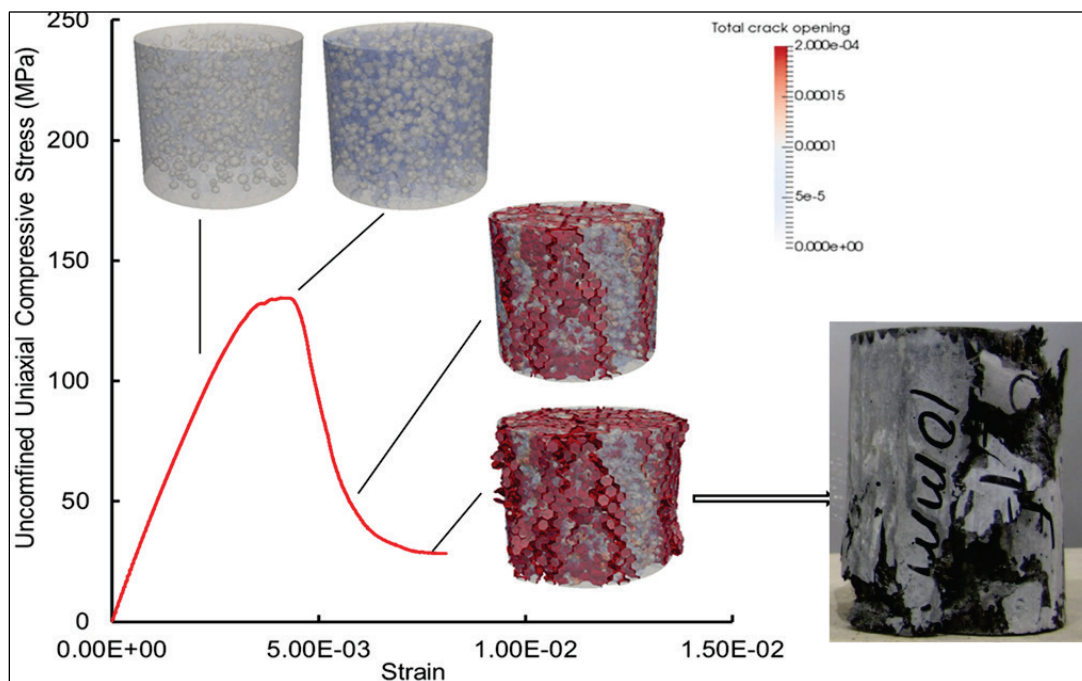
Figure 7. The stress/strain curve and corresponding snapshots of crack opening for specimens with mesopores under uniaxial compression.
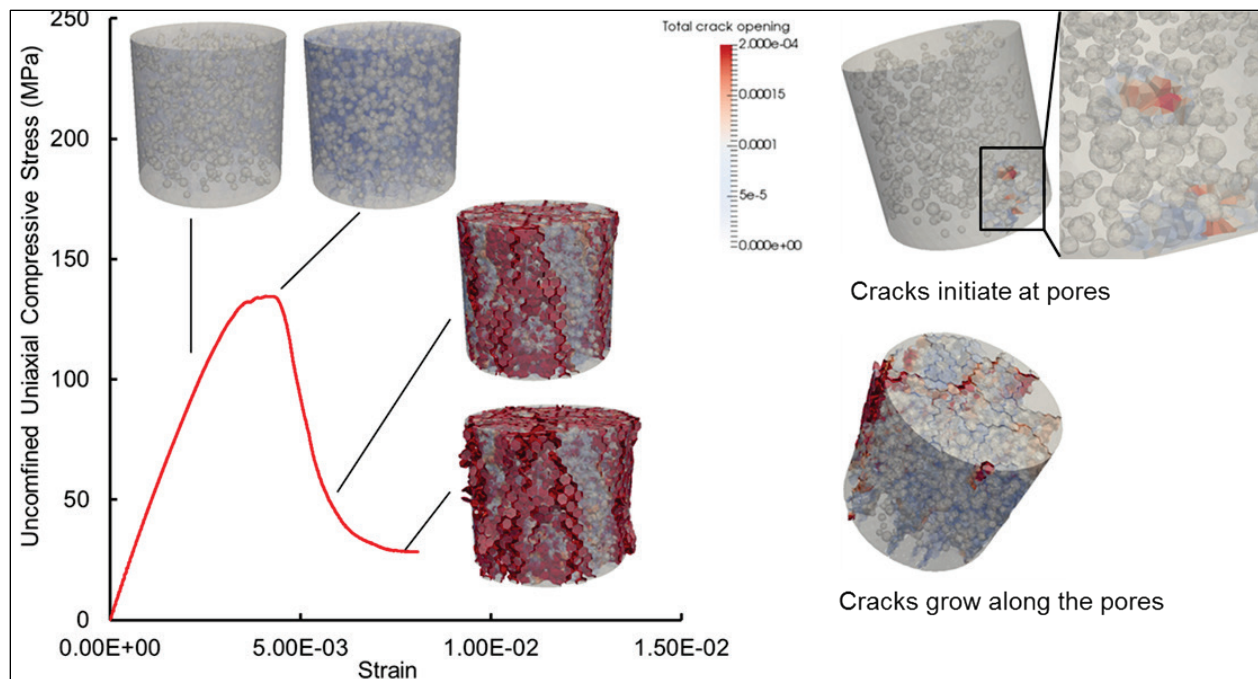
Figure 8. The stress/strain curve and corresponding snapshots of crack opening for specimens without mesopores under uniaxial tension.

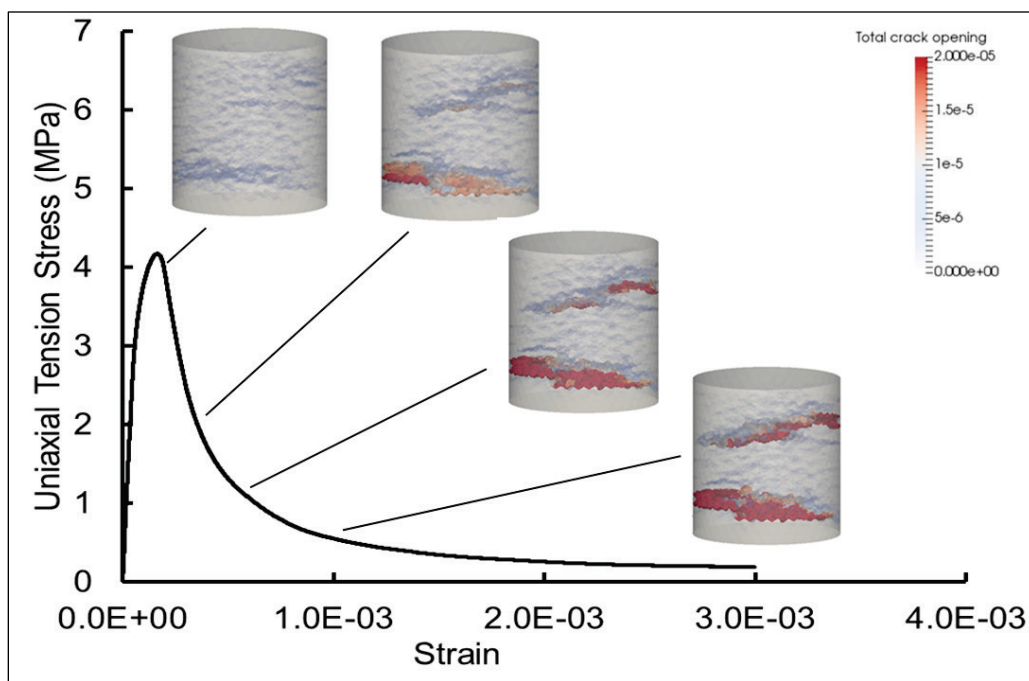Figure 9. The stress/strain curve and corresponding snapshots of crack opening on the specimens with mesopores under uniaxial tension.
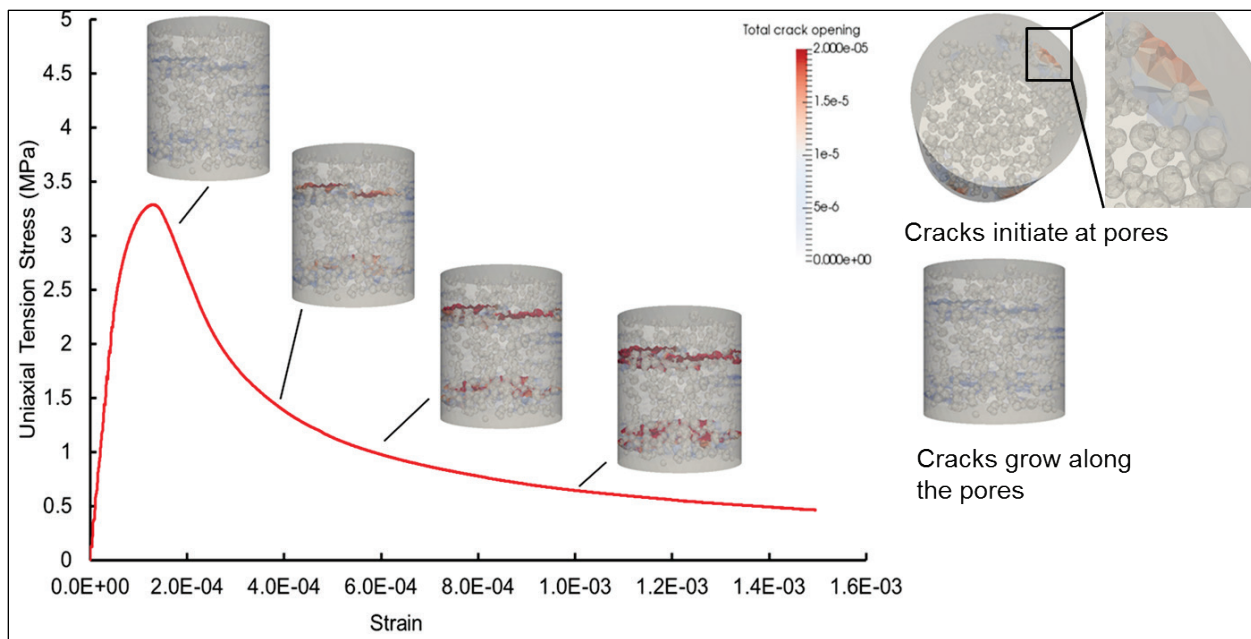
Figure 10. A comparison of stress/strain curves from LDPM simulation results for specimens with and without mesopores under uniaxial compression.
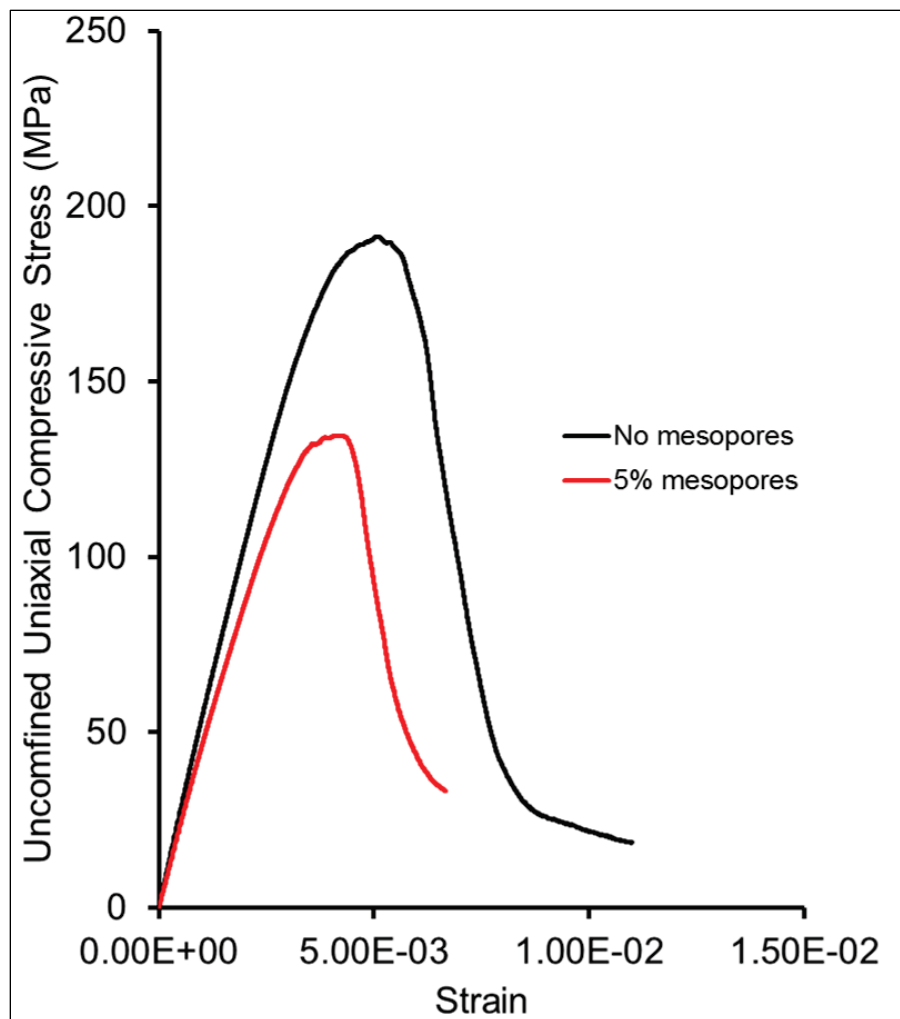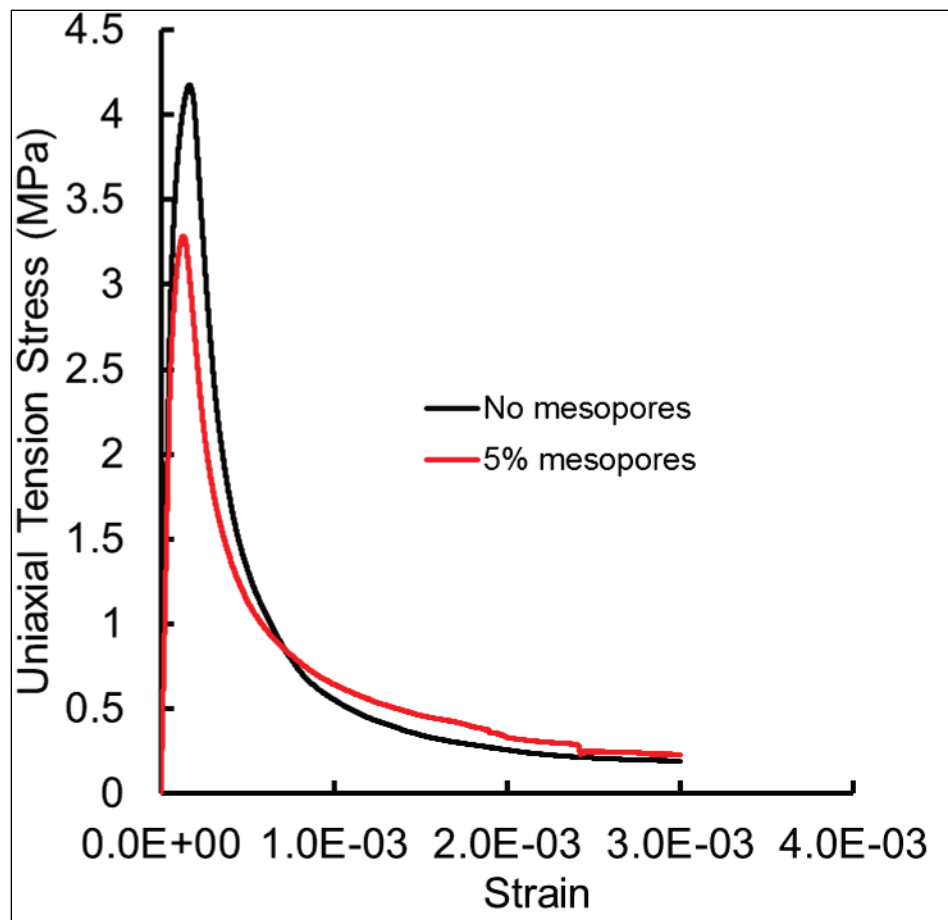
Figure 11. A comparison of stress/strain curves from LDPM simulation results for specimens with and without mesopores under uniaxial tension.

3   Mesoscale Modeling with the FEM

Mesoscale modeling with the FEM treats concrete as a two-phase material: aggregates and mortar. Same constitutive equations with different parameters are applied to different phases. Failure is based on a continuum damage mechanics concept. This approach is applied to a normal-strength concrete SAM 21 developed by ERDC. This chapter details the methods used to build a representative volume element (RVE) of concrete including the aggregate information from experiments and preliminary simulation results.

3.1   Finite-element mesh generation

Two methods were developed to generate an RVE of concrete, including aggregate information from experiments. The first is the classical approach of using primitive geometrical approximations for aggregate dispersed inside concrete while the second approach directly translates microstructure output from Virtual Cement and Concrete Testing Laboratory (VCCTL) simulations into a voxel-based mesoscale finite element mesh.

3.1.1   Primitive geometry approach

The first method approximated aggregate geometry as solid homogeneous spheres encased in homogeneous concrete mortar. The spheres were generated using the Virtual Composite Structure Generator (VCSG) (Lawrimore et al. 2016). The VCSG algorithm generates a randomized composite material structure that can then be used in computational simulations. Using the Box-Muller method (Box and Muller 1958), spheres were generated with diameters sampled at random from an experimentally determined distribution of aggregate sizes. The generated spheres were then inserted into an RVE by using Random Sequential Absorption (RSA) (Spencer and Sweeney 2008). RSA fills a volume by inserting objects at randomly generated coordinates subject to satisfying some criteria. The criteria can vary, but, in this case, the only criterion was that neighboring objects cannot intersect with each other.

3.1.1.1 VCSG walk-through

This section contains a step-by-step explanation of the VCSG algorithm tailored to the mesoscale concrete problem.

- Step 1. Define a distribution of spherical particle diameters from which to randomly sample.

  A sieve analysis was performed on crushed limestone used in SAM 21 concrete developed by ERDC. The gradation data were then converted to a volume fraction distribution using the aggregate diameters. Figure 12 shows the original gradation along with the resulting volume distribution.

Figure 12. Sieve analysis gradation curve (left) and resulting volume distribution (right) for different particle diameters.
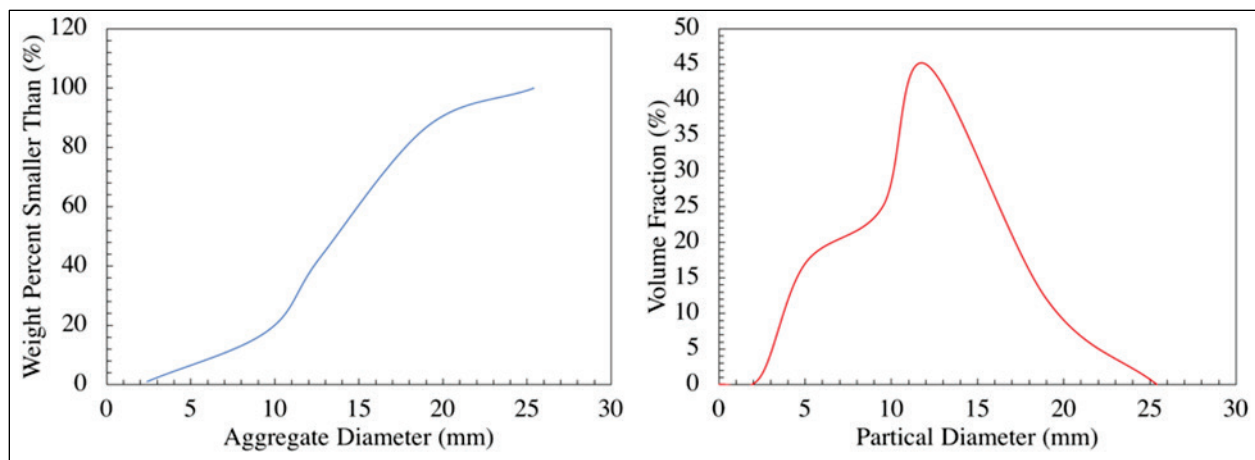
- Step 2. Determine domain geometry and dimensions. If the domain is an RVE, additional considerations, such as periodic boundary conditions, may need to be taken into account to achieve convergence.

  A cubic RVE with all sides having a length of 50 mm was used. The diameter of cylindrical samples tested by Akers and Phillips (2004) is 50 mm. The cubic RVE was large enough to fit all aggregate sizes while also being small enough not to overstress computing resources.

- Step 3. Run RSA algorithm to fill the domain laid out in Step 2 with spherical particles whose diameters are sampled from the distribution defined in Step 1.

  The Box-Mueller method was used to generate random samples from a Gaussian distribution. Figure 13 shows a sample RVE filled with spherical particles generated with RSA.

Figure 13. Cubic representative volume element filled with spheres sampled at random from a Gaussian distribution.
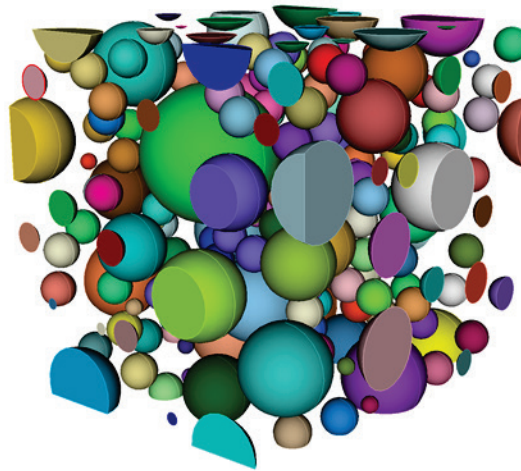
- Step 4. Generate a mesh for the completed domain.

The automated mesh generation toolkit CUBIT from Sandia National Laboratory (Blacker et al. 2016) was used to generate a mesh. Figure 14 displays the resulting mesh generated with CUBIT's "parallel-sculpt" method (Lim et al. 2015). The number of elements generated is nearly one million.

Figure 14. Hexahedral mesh generated with CUBIT for a cubic representative volume element containing spherical aggregate.
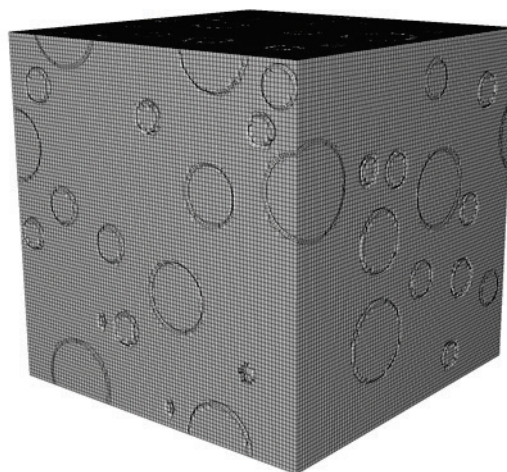
3.1.2   Direct translation from hydration simulations approach

The second approach is to translate concrete phase information from VCCTL (virtual cement and concrete testing laboratory [Sahachaiyunta et al. 2012; Bullard et al. 2009]) directly into a finite element model, as shown in Figure 15.

VCCTL is an interactive tool developed by the National Institute of Standards and Technology (NIST) that exploits user inputs related to concrete mix design to produce two-dimensional "slide" images of concrete topology approximated in two-dimensional quadrilaterals containing individual concrete phase IDs (two-dimensional voxels). Figure 16 shows an illustration of a slide from VCCTL. Translating the VCCTL slides into a finite element mesh consisted of generating nodes at each quadrilateral vertex in each slide and then extruding each two-dimensional quad to the next adjacent slide to create a three-dimensional hexahedral mesh. The following section contains a more detailed description of the process used to translate VCCTL slides into a finite element mesh.

Figure 15. Visualization of slides generated from VCCTL (left) and the resulting finite element mesh that was produced (right).
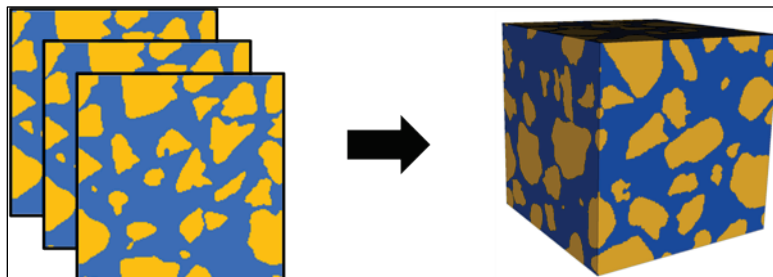
Figure 16. Illustration of a VCCTL "slide" showing multiple concrete phases.
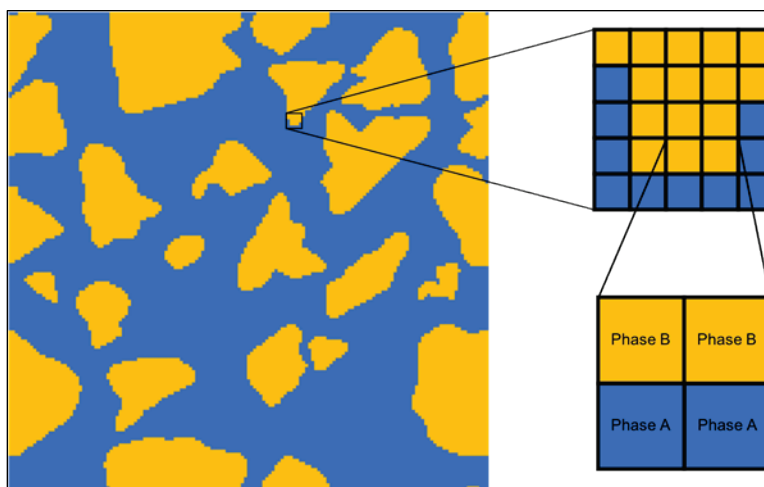
3.1.2.1 VCCTL data interpreter walk-through

Conceptually, the process of transforming VCCTL slides into a 3-D hexahedral finite element mesh is very simple. However, depending on the size of the material domain, the process can be laborious, possibly requiring high-performance computing resources. This walk-through assumes that a collection of VCCTL slides for conversion has been produced and that each quadrilateral in the slides has equivalent sides with a unit length.

Step 1. For each slide, a nodal point (x_1, x_2) with a new nodal index (i) at each vertex of each quadrilateral (Figure 17) is generated. For the third spatial coordinate(x_3), the number of the current slide being processed is used. For example, $x_3 = 1$ is used for the first slide, and $x_3 = 5$ is used for the fifth slide. As nodes are generated, they are stored in an ordered list as follows.

$$A_1 = \left[i_1 \ x_1^{i_1} \ x_2^{i_1} \ x_3^{i_1} \right]$$

$$A_2 = \left[i_2 \ x_1^{i_2} \ x_2^{i_2} \ x_3^{i_2} \right]$$

$$\vdots \ \vdots$$

$$A_n = \left[i_n \ x_1^{i_n} \ x_2^{i_n} \ x_3^{i_n} \right] \qquad\qquad 3.1$$

where A is the list of all nodes, and n is the total number of nodes.

Figure 17. Illustration of nodal locations at the vertices of each quadrilateral within a VCCTL slide.
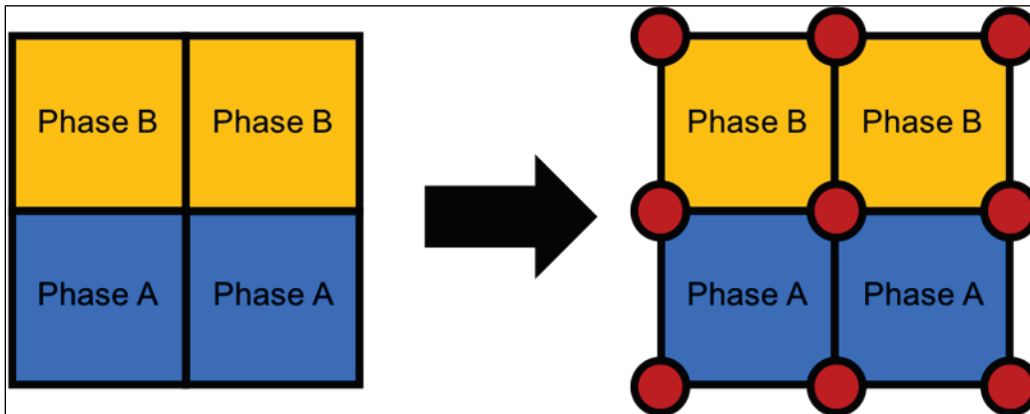
An additional full layer of nodes needs to be generated at either $x_3 = 0$ or $x_3 = L + 1$ in order to form the first or last layer of elements, respectively, where L is the total number of slides as well as the length of one side of the RVE.

Step 2. The location of the extra layer of nodes determines the direction of hexahedral element extrusion. Here, it is assumed that the extra layer of nodes was added at $x_3 = 0$. For each phase ID, the phase ID's location within the slide was used to determine which nodes "belonged" to the extruded hexahedral. For example, the phase ID in row r and column c of slide s needs the following nodes.

$$n_1 = [x_1 \; y_1 \; z_1]$$

$$n_2 = [x_2 \; y_1 \; z_1]$$

$$n_3 = [x_2 \; y_2 \; z_1]$$

$$n_4 = [x_1 \; y_2 \; z_1]$$

$$n_5 = [x_1 \; y_1 \; z_2]$$

$$n_6 = [x_2 \; y_1 \; z_2]$$

$$n_7 = [x_2 \; y_2 \; z_2]$$

$$n_8 = [x_1 \; y_2 \; z_2] \qquad\qquad 3.2$$

where x_i, y_i, and z_i are components of the spatial coordinates of the vertices of a hexahedral element and are given by

$$x_1 = r, y_1 = c, z_1 = s$$

$$x_2 = x_1 - 1, y_2 = y_1 - 1, z_2 = z_1 - 1 \qquad\qquad 3.3$$

Note that nodes $n_1 - n_8$ should be ordered according to the conventions of the finite element code that is intended for use. In this case, the nodes were ordered in accordance with the conventions of the structural finite element code DYNA3D.

Step 3. For each local node $(n_1 - n_8)$, the global list of nodes (A) generated in step 1 is searched for the correct global node index that corresponds to the coordinates from the local node. Once all eight global indices have been collected, a new global element index, e_i, is generated and stored alongside the eight corresponding nodes as follows.

$$E(1) = \left[e_1 \; p_1 \; n_1^{e_1} \; n_2^{e_1} \; n_3^{e_1} \; n_4^{e_1} \; n_5^{e_1} \; n_6^{e_1} \; n_7^{e_1} \; n_8^{e_1} \right]$$

$$E(2) = \left[e_2 \; p_2 \; n_1^{e_2} \; n_2^{e_2} \; n_3^{e_2} \; n_4^{e_2} \; n_5^{e_2} \; n_6^{e_2} \; n_7^{e_2} \; n_8^{e_2} \right]$$

$$\vdots \; \vdots$$

$$E(n) = \left[e_n \; p_n \; n_1^{e_n} \; n_2^{e_n} \; n_3^{e_n} \; n_4^{e_n} \; n_5^{e_n} \; n_6^{e_n} \; n_7^{e_n} \; n_8^{e_n} \right] \qquad 3.4$$

where p_i is a phase identifier. Again note that in this case, DYNA3D formatting conventions have been used. Figure 18 shows the resulting finite element mesh generated by using the algorithm described above. The number of elements is nearly four million.

Figure 18. Finite element mesh created from upscaling VCCTL slides.
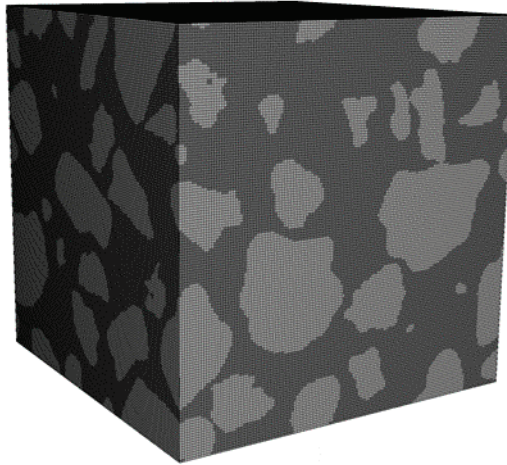
3.2 Material model and boundary conditions

Each finite element mesh generated in section 3.1 included two distinct materials: aggregate and mortar. The constitutive behavior of both materials was described by the Karagozian & Case (K&C) concrete material model (Malvar et al. 1997). The implementation of the K&C model within ParaDyn allows for an automatic fitting of model parameters using only the unconfined compressive strength of the material. The auto-calibration

feature was applied to fit the material parameters for both materials used in both finite element models. The aggregate was calibrated by using an unconfined compressive strength of 20 ksi while the mortar phase was calibrated with 1.2 ksi as an unconfined compressive strength. Note that these numbers were used only for illustration of the methods. In the future, the triaxial compression test results of mortar and aggregate from SAM21 will be used to fit the parameters based on K&C concrete model.

All finite element meshes developed in section 3.1 were subjected to unconfined uniaxial compression. All simulations were executed by using the parallelized form of DYNA3D (ParaDyn) from Lawrence Livermore National Laboratory (Zywicz and Lin 2015).

3.3   Results and discussion

Figure 19 shows the damage states of each finite element mesh under quasi-static uniaxial unconfined compressive load. In both models, damage is concentrated at the interfaces between aggregate and cement paste. Note the simulation results are for demonstration only. In the future, the material parameters fitted from experimental data will be applied to the FEM models for more accurate simulations.

Figure 19. Contour plots showing damage for the geometrically primitive mesh (left) and the mesh resulting from the direct translation from VCCTL (right). Note the red color indicates a higher damage level than that of surrounding materials.
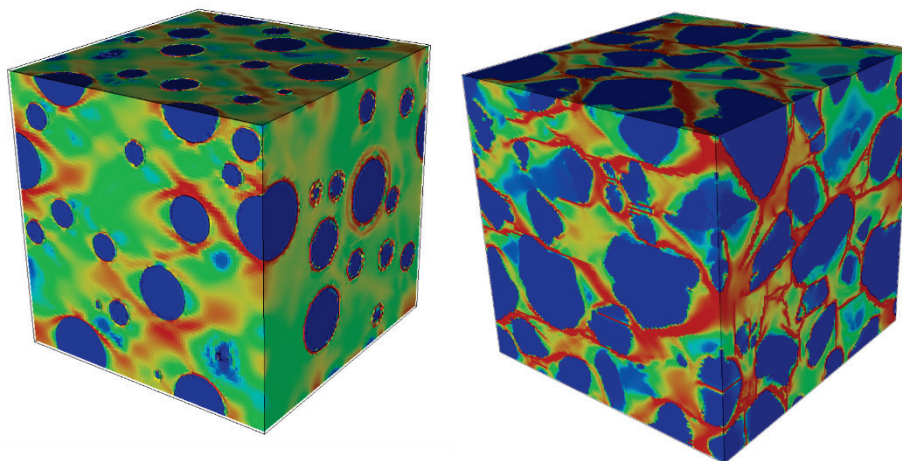
4 Summary and Future Work

In this report, we examined the basic features of the Lattice Discrete Particle Method (LDPM) and the Finite Element Method (FEM) applied for mesoscale simulations. We also performed mesoscale simulations of UHPC based on the LDPM and illustrated the procedures of building mesoscale finite element concrete models of a normal-strength concrete, including the detailed information of aggregate and mortar.

The current LDPM implementation treats aggregates as rigid spheres; the fracture was assumed to occur at the mortar region. The constitutive equations were applied on the facets between aggregates to describe the elastic/plastic responses, pore collapse, compaction, and damage; and the model parameters were fitted from a number of standard laboratory tests. This implementation can model cracking between aggregates naturally, as illustrated in the previous chapter. As shown in the previous chapter, porosities at similar size scales of aggregates can also be explicitly modeled in the LDPM, and the simulations can capture the effects of pores on the fracture. The current LDPM implementation is computationally efficient and is designed to model structure responses. Experiments (Nemati 1997) indicated that fracture in concrete often initiates from ITZ and connects with pores, and it can also grow through the aggregates, particularly at a high strain rate. In order to capture the mechanisms such as microcracking at the ITZ, fracturing of mortar and aggregate, and also to take into account the shapes of aggregates, both mortar and aggregates need to be discretized into multiple particles; the particle interactions need to be formulated based on individual phase properties of mortar, aggregates, and the ITZ. The number of particles in these models will increase exponentially. RVE, instead of full specimen size, may need to be modeled.

Mesoscale finite element simulations outlined in the report modeled concrete as two-phase materials, and models took into account the size, shape, and distribution of the aggregates. In the future, the ITZ will be included in the model as a separate phase or as an interface. As shown in the previous chapter, the number of elements is very large in order to include enough aggregates in the RVE. Size scale analysis needs to be performed to investigate the appropriate RVE size. A concrete damage-plasticity model can be applied to all three phases, and model parameters can be calibrated from experimental data for each individual phase.

Damage can occur in the mortar, the ITZs, and the aggregates. Akers and Phillips (2004) performed triaxial tests on aggregates, mortar, and concrete. These data will be used to fit the parameters of material models applied to different phases.

Both LDPM and FEM are viable methods in modeling concrete at mesoscale. Future work will include performing simulations based on the laboratory tests such as unconfined compression, triaxial compression, and hydrostatic compression. These simulations will test the robustness of these methods, provide information about the appropriate RVE sizes, and verify the applied constitutive laws and associated material constants. Once the methods and models are verified, the different stress states, strain paths, and loading rates will be applied on the models to support the development of macroscale constitutive laws. The parametric studies will also be performed to investigate the effects of size distribution, volume fraction and shape of the aggregates on the mechanical properties and responses of the concrete, which will pave the way for optimizing concrete at mesoscale for military and civilian applications.

To associate the mesoscale material behavior with the materials process parameters such as selections of cement, water/cement ratio, and additive materials, the material models and parameters applied in the FEMs for the mortar and the ITZ phases need to be linked with the structure and mechanisms at the lower length scale via microscale simulations. The particle interaction laws and parameters applied in the LDPM models for mortar and the ITZ also need to be derived from microscale simulations.

References

Adley, M., A. Frank, K. Danielson, S. Akers, and J. O'Daniel. 2010. *The advanced fundamental concrete (AFC) model*. ERDC/GSL TR-10-51. Vicksburg, MS: U.S. Army Engineer Research and Development Center.

Akers, S. A., and B. R. Phillips. 2004. *Concrete modeled as an inhomogeneous material: Numerical simulations of contact detonations charges*. 18th International Symposium on Military Aspects of Blast and Shock, 27 September-1 October, Bad Reichenhall, Germany, 51-53.

Allen A. J., J. J. Thomas, and H. M. Jennings. 2007. Composition and density of nanoscale calcium-silicate-hydrate in cement. *Nature Material* 6:311-315.

Ashari, S. E., G. Buscarnera, and G. Cusatis. 2017. A lattice discrete particle model for pressure-dependent inelasticity in granular rocks. *International Journal of Rock Mechanics Mining Sciences* 91:49-58.

Bazant, Z. P., F. C. Caner, I. Carol, M. D. Adley, and S. A. Akers. 2000. Microplane model M4 for concrete I: Formulation with work-conjugate deviatoric stress. *Journal of Engineering Mechanics* 126 (9):944-953.

Bentz, D. P. 2005. Quantitative comparison of real and CEMHYD3D model microstructures using correlation functions. *Cement and Concrete Research* 36:259-263.

Blacker, T., S. J. Owen, M. L. Staten, R. W Quadros, B. Hanks, B. Clark, R. J. Meyers, C. Ernst, K. Merkley, R. Morris, C. McBride, C. Stimpson, M. Plooster, and S. Showman. 2016. *CUBIT: Geometry and mesh generation toolkit 15.2 user documentation*. SAND2016-1649R. Albuquerque, NM: Sandia National Laboratories.

Box, G. E. P., and M. E. Muller. 1958. A note on the generation of random normal deviates. *The Annals of Mathematical Statistics* 29(2): 610-11. doi:10.1214/aoms/1177706645.

Bullard, J. W., P. E. Stutzman, L. M. Ordoñez-Belloc, E. J. Garboczi, and D. P. Bentz. 2009. Virtual cement and concrete testing laboratory for quality testing and sustainability of concrete. *Modeling as a Solution to Concrete Problems,* 266:27-36.

Burcham, M. N. 2016. Multiscale structure-property relationships of ultra-high performance concrete. MS thesis, Mississippi State University.

Calixto, J. M. 2001. Microcracking of high performance concrete subjected to biaxial tension-compression stresses. *Materials Research* 5(3):295-299.

Canner, F. C., and Z. P. Bazant. 2000. Microplane model M4 for concrete. II: Algorithm and calibration. *Journal of Engineering Mechanics* 126(8):954-961.

Cusatis, G., Z. Bazant, and L. Cedonlin. 2003. Confinement-shear lattice model for concrete damage in tension and compression: I. Theory. *Journal of Engineering Mechanics* 129(12):1439-1448.

Cusatis, G., D. Pelessone, and A. Mencarelli. 2011. Lattice Discrete Particle Model (LDPM) for failure behavior of concrete. I: Theory. *Cement & Concrete Composites* 33:881-890.

Fossum, A., and R. Brannon. 2016. On a viscoplastic model for rocks with mechanism-dependent characteristic times. *ActaGeotech* (1):89-106.

Jin, L., J. Yu, R. Zhang, and X. Du, Xiuli. 2017. Numerical study on the impact performances of reinforced concrete beams: A mesoscopic simulation method. *Engineering Failure Analysis* (80):141-163.

Landis, E. N., R. Kravchuk, and D. Loshkov. 2019. Experimental investigations of internal energy dissipation during fracture of fiber-reinforced ultra-high-performance concrete. *Frontiers of Structural and Civil Engineering* 13(1):190-200.

Lawrimore, W. B., B. Paliwal, M. Q. Chandler, K. L. Johnson, and M. F. Horstemeyer. 2016. Hierarchical multiscale modeling of polyvinyl alcohol/montmorillonite nNanocomposites. *Polymer* 99:386-98. doi:10.1016/j.polymer.2016.07.026.

Lim, H., S. Owen, F. Abdeljawad, B. Hanks, and C. Battaile. 2015. *Creating physically-based three-dimensional microstructures : Bridging phase-field and crystal plasticity models*. Sandia Report SAND2015-7870. Albuquerque, NM: Sandia National Laboratory.

Lin, S.-P., J.-S. Chen, and S. Liang. 2016. A damage analysis for brittle materials using stochastic micro-structural information. *Computational Mechanics* (57):371-385.

Liu, D., B. Šavija, G. Smith, P. E. Flewit, T. Lowe, and E. Schlangen. 2017. Towards understanding the influence of porosity on mechanical and fracture behaviour of quasi-brittle materials: experiments and modelling. *International Journal of Fracture* 205(1):57-72.

Malvar, L. J., J. E. Crawford, J. W. Wesevich, and D. Simons. 1997. A plasticity concrete material model for DYNA3D. *International Journal of Impact Engineering* 19(9):847-73. doi: 10.1016/S0734-743X(97)00023-7.

Mayercsik, N. P. 2015. Characterization of multiscale porosity in cement-based materials: Effects of flaw morphology on material response across size and time scales. PhD diss., Georgia Institute of Technology.

Mehta, P. K., and J. M. Monteiro. 2014. *Concrete: Microstructure, properties, and materials*. 4th ed. New York: McGraw Hill Professional, Access Engineering.

Mencarelli, Andrea. 2007. The Lattice Discrete Particle Model (LDPM) for concrete: Calibration and validation under quasi-static loading conditions. MS thesis, Rensselaer Polytechnic Institute.

Moser, R. D., P. G. Allison, and M. Q. Chandler. 2013. Characterization of impact damage in ultra-high performance concrete using spatially correlated nanoindentation/sem/edx. *Journal of Materials Engineering and Performance* 22:3902-3908.

Nemati, K. 1997. Fracture analysis of concrete using scanning electron microscopy. *Scanning: The Journal of Scanning Microscopies* 19(6):426-430.

Oesch, T. 2016. *In Situ CT investigation of pull-out failure for reinforcing bars embedded in conventional and high-performance concretes*. 6th Conference on Industrial Computed Tomography. Wels, Austria.

Paliwal, B., and K. T. Ramesh. 2008. An interacting micro-crack damage model for failure of brittle material under compression. *Journal of the Mechanics and Physics of Solids* (56):896-923.

Qsymah, A., R. Sharma, Z. Yang, L. Margetts, and P. Mummery. 2017. Micro X-ray computed tomography image-based two-scale homogenization of ultra-high performance fiber reinforced concrete. *Construction and Building Materials* (130):230-240.

Ren, X., J.-S. Chen, J. Li, T. R. Slawson, and M. J. Roth. 2010. Micro-cracks informed damage models for brittle solids. *International Journal of Solids and Structures* (48):1560-1571.

Sahachaiyunta, P., K. Pongpaisanseree, J. W Bullard, P. E Stutzman, E. J. Garboczi, and W. Vichit-Vadakan. 2012. Virtual testing in a cement plant: A tool for producing customized products. *Concrete International* September:33-39.

Schlangen, E., and E. J. Garboczi. 1997. Fracture simulations of concrete using lattice models: Computational aspects. *Engineering Fracture Mechanics* 57(2/3):319-332.

Scott, D. A., W. R. Long, R. D. Moser, B. H. Green, J. L. O'Daniel, and B. A. Williams. 2015. *Impact of steel fiber size and shape on the mechanical properties of ultra-high performance concrete*. ERDC/GSL TR-15-22. Vicksburg, MS: U.S. Army Engineer Research and Development Center.

Sinaie, S. 2017. Application of the discrete element method for the simulation of size effects in concrete samples. *International Journal of Solids and Structures* (108):244-253.

Spencer, P. E., and J. Sweeney. 2008. Modeling of polymer clay nanocomposites for a multiscale approach. *ArXiv: 0809.0888 [cond-mat.mtrl]*. doi: 10.1016/j.compositesb. 2011.12.012.

Suchorzewski, J., J. Tejchman, and M. Nitka. 2017. Discrete element method simulations of fracture in concrete under uniaxial compression based on its real internal structure. *International Journal of Damage Mechanics* 27(4):578-607.

Vegt, I., K. van Brenugel, and J. Weerheijm. 2007. Failure mechanisms of concrete under impact loading. In *Fracture mechanics of concrete and concrete structures*, d. by A. Carpinteri, P. Gambarova, G. Ferro, and G. Plizzari, 579-587. London: Taylor & Francis Group.

Williams, E. M., S. S. Graham, S. A. Akers, P. A. Reed, and T. S. Rushing. 2010. Constitutive property behavior of an ultra-high-performance concrete with and without steel fibers. *Computers and Concrete* 7(2):191-200.

Williams, E. M., S. S. Graham, P. A. Reed, and T. R. Rushing. 2009. *Laboratory characterization of Cor-Tuf concrete with and without steel fibers*. ERDC/GSL TR-09-22. Vicksburg, MS: U.S. Army Engineer Research and Development Center.

Zhou, R., Z. Song, Zhenhuan, and Y. Lu. 2017. 3D mesoscale finite element modeling of concrete. *Computers and Structures* 192:96-113.

Zywicz, E., and J. I. Lin. 2015. *DYNA3D: A nonlinear explicit three-dimensional finite element code for solid and structural mechanics: Version 15*. LLNL-SM-678186. Livermore, CA: Lawrence Livermore National Laboratory.

REPORT DOCUMENTATION PAGE		*Form Approved* *OMB No. 0704-0188*
Public reporting burden for this collection of information is estimated to average 1 hour per response, including the time for reviewing instructions, searching existing data sources, gathering and maintaining the data needed, and completing and reviewing this collection of information. Send comments regarding this burden estimate or any other aspect of this collection of information, including suggestions for reducing this burden to Department of Defense, Washington Headquarters Services, Directorate for Information Operations and Reports (0704-0188), 1215 Jefferson Davis Highway, Suite 1204, Arlington, VA 22202-4302. Respondents should be aware that notwithstanding any other provision of law, no person shall be subject to any penalty for failing to comply with a collection of information if it does not display a currently valid OMB control number. **PLEASE DO NOT RETURN YOUR FORM TO THE ABOVE ADDRESS.**		

1. REPORT DATE *(DD-MM-YYYY)* May 2019	2. REPORT TYPE Final	3. DATES COVERED *(From - To)*

4. TITLE AND SUBTITLE Mesoscale Modeling of Cementitious Materials: Phase I	5a. CONTRACT NUMBER
	5b. GRANT NUMBER
	5c. PROGRAM ELEMENT NUMBER
6. AUTHOR(S) Mei Qiang Chandler, William B. Lawrimore, Micael C. Edwards, Robert D. Moser, Jameson D. Shannon, and James L. O'Daniel	5d. PROJECT NUMBER 465387
	5e. TASK NUMBER
	5f. WORK UNIT NUMBER

7. PERFORMING ORGANIZATION NAME(S) AND ADDRESS(ES) Geotechnical and Structures Laboratory U.S. Army Engineer Research and Development Center 3909 Halls Ferry Road Vicksburg, MS 39180-6199	8. PERFORMING ORGANIZATION REPORT NUMBER ERDC/GSL TR-19-25

9. SPONSORING / MONITORING AGENCY NAME(S) AND ADDRESS(ES) U.S. Army Corps of Engineers Washington, DC 20314-1000	10. SPONSOR/MONITOR'S ACRONYM(S) USACE
	11. SPONSOR/MONITOR'S REPORT NUMBER(S)

12. DISTRIBUTION / AVAILABILITY STATEMENT
Approved for public release; distribution is unlimited.

13. SUPPLEMENTARY NOTES

14. ABSTRACT
Cementitious materials such as concrete are intrinsically heterogeneous and include internal structures and constituents across length scales ranging from nanometers to millimeters. These materials are widely used as protective materials for military applications. They need not only to withstand conventional quasi-static loadings but also to defeat extreme loadings such as high-rate blast, impact, and penetration. To fully explore the design and application of these materials in war-fighting efforts, it is essential to understand the deformation and failure mechanisms of multiscale internal structures and constituents under different loading conditions. Mesoscale structures and constituents of cementitious materials include mesoscale particles such as aggregates, sand, fibers, mesoscale porosities, and cracks. Several numerical methods have been developed to investigate the deformation and failure mechanisms of mesoscale structures and constituents under different loading conditions. In this report, we explored the Lattice Discrete Particle Method (LDPM) and the Finite Element Method (FEM). The work provides some basic knowledge on these methods and aids in formulating a path forward in the next phase of the research.

15. SUBJECT TERMS	Mesoscale modeling	Constitutive laws
Concrete	Lattice Discrete Particle Modeling (LDPM)	Cement composites
Mechanical properties	Finite Element Modeling (FEM)	Materials science

16. SECURITY CLASSIFICATION OF:			17. LIMITATION OF ABSTRACT	18. NUMBER OF PAGES	19a. NAME OF RESPONSIBLE PERSON
a. REPORT	b. ABSTRACT	c. THIS PAGE			
Unclassified	Unclassified	Unclassified		39	19b. TELEPHONE NUMBER *(include area code)*

Standard Form 298 (Rev. 8-98)
Prescribed by ANSI Std. 239.18